# Gamma-Ray Bursts Calibrated from the Observational H(z) Data in Artificial Neural Network Framework

Zhen Huang<sup>a,c,1</sup>, Zhiguo Xiong<sup>a</sup>, Xin Luo<sup>a</sup>, Guangzhen Wang<sup>a</sup>, Yu Liu<sup>b,\*\*</sup>, Nan Liang<sup>a,\*</sup>

<sup>a</sup>Guizhou Key Laboratory of Advanced Computing, Guizhou Normal
 University, Guiyang, 550025, Guizhou, China
 <sup>b</sup>School of Physical Science and Technology, Southwest Jiaotong University, Chengdu, 611756, Sichuan, China
 <sup>c</sup>School of Cyber Science and Technology, Guizhou Normal University, Guiyang, 550025, Guizhou, China

#### Abstract

In this paper, we calibrate the luminosity relation of gamma-ray bursts (GRBs) from an Artificial Neural Network (ANN) framework for reconstructing the Hubble parameter H(z) from the latest observational Hubble data (OHD) obtained with the cosmic chronometers method in a cosmology-independent way. We consider the physical relationships between the data to introduce the covariance matrix and KL divergence of the data into the loss function and calibrate the Amati relation ( $E_{\rm p}$ - $E_{\rm iso}$ ) by selecting the optimal ANN model with the A219 sample and the J220 sample at low redshift. Combining the Pantheon+ type Ia supernovae (SNe Ia) sample and Baryon acoustic oscillations (BAOs) from Dark Energy Spectroscopy Instrument (DESI) with GRBs at high redshift in the Hubble diagram by Markov Chain Monte Carlo numerical method, we find that the  $\Lambda$ CDM model is preferred over the wCDM and CPL models with joint constraints by the Akaike Information Criterion and Bayesian Information Criterion.

Keywords: gamma-ray bursts: general - (cosmology:) dark energy - cosmology: observations

### 1. Introduction

Gamma-ray bursts (GRBs) are the most powerful high-energy phenomena in the universe, which can be used to probe the universe up to  $z\sim 9$  (Salvaterra et al. , 2009; Cucchiara et al., 2011), far exceeding the maximum redshift of Type Ia supernovae (SNe Ia) at  $z\sim 2$  (Scolnic et al., 2018, 2022). The luminosity relations of GRBs (Amati et al., 2002; Ghirlanda et al., 2004a; Yonetoku et al., 2004; Liang & Zhang, 2005; Dainotti et al., 2008, 2016; Izzo et al., 2015) have enabled their use as cosmological tools (Dai et al., 2004; Ghirlanda et al., 2004b; Liang & Zhang, 2006; Ghirlanda et al., 2006; Schaefer, 2007; Wang et al., 2015; Dainotti & Amati, 2018; Luongo & Muccino, 2021a; Han et al., 2024; Li et al., 2024; Bargiacchi et al., 2025) and Hu et al. (2021); Wang et al. (2022); Cao et al. (2022a,b). In early studies, the luminosity relations usually calibrated by assuming a specific cosmological model due to the absence of a low-redshift GRB sample (Dai et al., 2004), which can introduce the circularity problem. Liang et al. (2008) proposed a model-independent calibration method by interpolating GRB data from low-redshift SNe Ia observations; therefore GRBs can be used to constrain cosmological parameters without assuming a prior cosmological model (Capozziello & Izzo, 2008, 2009; Wei & Zhang, 2009; Wei, 2010; Liang et al., 2010, 2011; Wang et al., 2016; Liu et al., 2022b).

<sup>\*</sup>Corresponding author. Email: liangn@bnu.edu.cn

<sup>\*\*</sup>Corresponding author. Email: lyu@swjtu.edu.cn

<sup>&</sup>lt;sup>1</sup>Email: zhen huang@gznu.edu.cn

Another strategy to mitigate the circularity problem is the simultaneous fitting method (Amati et al., 2008; Wang, 2008), where the parameters of the GRB relations and the cosmological model are determined jointly. Recent findings suggest that the GRB relation parameters remain consistent across different cosmological models, implying that GRB data can be standardized within error margins (Khadka & Ratra, 2020). GRB luminosity relations can also be calibrated using other observational datasets. For instance, Amati et al. (2019) employed the observational Hubble data (OHD) derived from the cosmic chronometers (CC) method and used a Bézier parametric curve to calibrate the GRB  $E_{\rm p}$ - $E_{\rm iso}$  correlation (commonly known as the Amati relation) (Amati et al., 2002) and constrain cosmological models (Montiel et al., 2021; Luongo & Muccino, 2021b, 2023; Muccino et al., 2023).

The calibration of GRBs using cosmological data can be approached in various reconstruction techniques: such as the interpolation technique (Liang et al., 2008; Liu et al., 2022b), polynomial fitting (Kodama et al., 2008), iterative procedures Liang & Zhang (2008), local regression techniques (Cardone et al., 2009; Demianski et al., 2017, 2021), cosmographic approaches (Capozziello & Izzo, 2010; Gao et al., 2012; Dai et al., 2021), two-step methods minimizing the reliance on SNe Ia (Izzo et al., 2015; Muccino et al., 2021), the Padé approximation (Liu & Wei, 2015), and the Bézier parametric approach (Amati et al., 2019). At the other hand, non-parametric methods, demonstrating superior accuracy in reducing the errors typically associated with the aforementioned techniques have been introduced to reconstruct from observational data. One of the most promising non-parametric approaches is the Gaussian Process (GP), which is a data smoothing technique grounded in Bayesian statistics. In recent years, the GP method has gained significant traction as a model-independent regression tool in cosmology, e.g., Seikel et al. (2012a,b); Li & Lin (2018); Pan et al. (2020); Li et al. (2021); Sun et al. (2021); Mu et al. (2023a,b) and Zhang et al. (2024a). However, GP faces several challenges to reconstruct  $H_0$  from observational data (Wei & Wu , 2017). Moreover, not all cosmological datasets follow a normal distribution, which can effect the reliability of reconstructed H(z) data (Zhang et al., 2024b).

Recently, it should be note that the potential use of machine learning (ML) algorithms for cosmological use with GRBs. ML are a set of technologies that learn to make predictions and decisions by training with a large amount of the observational data, which are a collection of processing units designed to identify underlying relationships in input data. The ML methods have shown outstanding performance in solving cosmological problems in both accuracy and efficiency to provide powerful tools and methods for cosmological research (Luongo & Muccino, 2021b). Zhang et al. (2025) used the Pantheon+ sample (Scolnic et al., 2022) to calibrate the Amati relation with ML approaches. Moreover, the concept of Artificial neural networks (ANN), completely driven by data, allows us to reconstruct a function from any kind of data without assuming a parametrization of the function. Wang et al. (2020) proposed an ANN approach for reconstructing functions from observational data with Hubble parameter measurements H(z)and the distance-redshift relation of SNe Ia. Escamilla-Rivera et al. (2020) used the Recurrent Neural Networks (RNN) and the Bayesian Neural Networks (BNN) to reduce the computation load of expensive codes for dark energy models; which have subsequently been used to calibrate the GRB relations (Escamilla-Rivera et al., 2022; Tang et al., 2021). Dialektopoulos et al. (2022) noted that another advantage of the ANN method is the ANN structure makes fewer assumptions than GP in this context, providing a more authentic representation of cosmological parameters. Gómez-Vargas et al. (2023) reconstructed cosmological functions using ANNs based on observational measurements with minimal theoretical and statistical assumptions with data from CC,  $f\sigma_8$  measurements, and SNe Ia. Zhang et al. (2024b) found that ANNs do not inherently rely on prior beliefs about the data distribution.

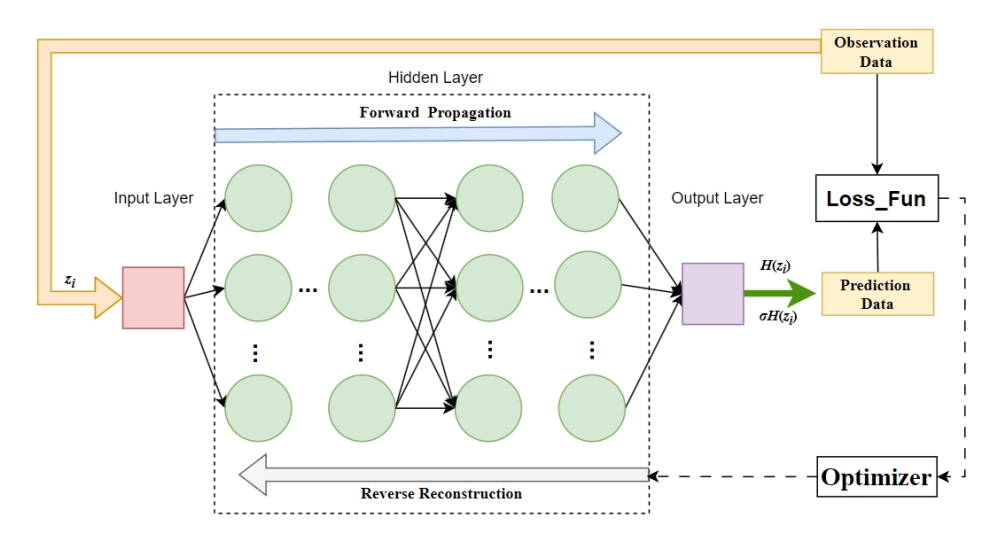


Figure 1: The structure of the ANN used in this work. The input is the redshift z of a Hubble parameter H(z), and the outputs are the predicted H(z) and  $\sigma_{H(z)}$  values. The thick arrows in the hidden layers represent the forward propagation of the data and the white arrows represent the reverse reconstruction of the error with the loss function.

Recently, Khadka et al. (2021) compiled the A220 sample in which the A118 sample with the smallest intrinsic dispersion. Liang et al. (2022) calibrated the Amati relation with the A219 sample updated from the A220 sample. Wang, Li & Liang (2024) constrained the emergent dark energy models with the A118 sample, OHD and baryon acoustic oscillation (BAO) data at intermediate redshift. Nong & Liang (2024) used the A118 GRB sample and the Pantheon+sample to test the phenomenological interacting dark energy model. More recently, Jia et al. (2022) tested the Amati relation by using 221 GRBs (the J221 sample) based on the previous data including 49 GRBs from Fermi catalog. Xie et al. (2024) used a GP approach to calibrate the Amati relation with the J221 sample from the Pantheon+ sample. Cao & Ratra (2024) used the updated J220 GRB sample from Jia et al. (2022) to simultaneously constrain Amati correlation parameters and cosmological parameters from a joint analysis of OHD and BAO data. Shah et al. (2024) used a novel deep learning framework called LADDER (Learning Algorithm for Deep Distance Estimation and Reconstruction) to reconstruct the cosmic distance ladder with the A219 sample.

In this paper, we propose an ANN framework to calibrate the Amati relation with the A219 sample (Liang et al., 2022; Khadka et al., 2021) and the J220 sample (Cao & Ratra, 2024; Jia et al., 2022) from the latest OHD at low redshift. Combining GRB data at high redshift with the Pantheon+ sample and BAOs, we constrain dark energy models in a flat space by the MCMC method.

#### 2. Reconstruction From ANN

In this paper, we consider the feedforward neural network (FFNN) with a structure consisting of input and output layers connected to a hidden layer or a series of successive hidden layers, where elements of each layer are called neurons. We show the structure of a neural network with L-layers in Fig. 1. The input layer consists of the features of the dataset, with each neuron representing a feature or variable. The output layer is mainly responsible for the output of the final result, the specific form of which depends on the task, whose value must be evaluated by the error function, also known as the loss function, which measures the difference between the predicted value of ANN and the actual value of the data set.

The neurons in the hidden layers for each layer receive the output of the neurons in the previous layer and output it to the neurons in the next layer. The hidden layer in ANN is responsible for neural network learning and data processing, which can have one or more layers. For each point in the input layer, the hidden layer performs a linear transformation (consisting of linear weights and biases) and nonlinear activation on it, and then passes the inferred results to the output layer. For the forward propagation in the hidden layers with L-layers, the output  $a^{(l)}$  at layer l is

$$a^{(l)} = f^{(l)} \left( W^{(l)} \mathbf{a}^{(l-1)} + b^{(l)} \right), \quad l = 1, 2, \dots, L$$
 (1)

here, f(x) is the activation function.<sup>2</sup> W and b represent the weights and the biases. In order to better minimize the difference between the predicted value  $\hat{Y}$  and the true value Y, we calculate a loss function  $(\mathcal{L})$  to measure the difference between the predicted value and the true value. When getting the value of the loss function, we need to pass the parameter and gradient information to an optimizer<sup>3</sup> which is responsible for the update of the network parameters in each iteration. For the reverse reconstruction in in the hidden layers, the weight and bias is updated by

$$W^{(l)} \leftarrow W^{(l)} - \eta \nabla W^{(l)} \mathcal{L}, \quad b^{(l)} \leftarrow b^{(l)} - \eta \nabla b^{(l)} \mathcal{L}, \tag{2}$$

here  $\eta$  refers to the learning rate.

ANNs can handle a wider range of data types, but still require careful design of the network structure and loss function. It should be noted that different loss functions will also affect the final prediction results. Wang et al. (2020) used the Mean Absolute Error (MAE)<sup>4</sup> as a loss function. Gómez-Vargas et al. (2023) used the values of the mean squared error (MSE)<sup>5</sup>. ANN will organize multiple target outputs into a tensor, and then sum (or average) their loss function values. However, it is not possible to simply add the two loss values when finding the loss function. Recently, Chen et al. (2024) used two sets of neural networks to train H(z)and their uncertainty individually. Shah et al. (2024) used KL divergence as a loss function to consider the physical meaning represented by H(z) and  $\sigma_{H(z)}$ . KL divergence can maintain consistency between the predicted and observed distributions, also known as relative entropy, is a method to describe the difference between two probability distributions, which defined as:

$$D_{\mathrm{KL}}(P||Q) = \sum_{i} P(i) \log \left(\frac{P(i)}{Q(i)}\right) \tag{3}$$

where P and Q are the true distribution and the fitting distribution.

<sup>&</sup>lt;sup>2</sup>In regression problems, the output layer uses the identity function, while hidden layers use nonlinear activation functions. We use the Exponential Linear Unit (ELU) (Clevert et al., 2015),  $f(x) = \begin{cases} x, & x > 0 \\ \alpha(e^x - 1), & x \le 0 \end{cases}$ where  $\alpha$  is a positive hyperparameter controlling the saturation for negative inputs, which are set to 1 for convenience.

<sup>&</sup>lt;sup>3</sup>There are four common optimizers: SGD, Momentum, AdaGrad, Adam. In our work, we adopt Adam (Kingma & Ba, 2014) as the optimizer, which can accelerate the update of parameters. However, it should be noted that the results will vary depending on the problem to be solved.

<sup>&</sup>lt;sup>4</sup>MAE without accounting for the data uncertainties is defined as:  $\text{MAE} = \frac{1}{N} \sum_{i=1}^{N} (H_{\text{obs}}(z_i) - H_{\text{pred}}(z_i)).$ <sup>5</sup>MSE without accounting for the data uncertainties is defined as:  $\text{MSE} = \frac{1}{N} \sum_{i=1}^{N} (H_{\text{obs}}(z_i) - H_{\text{pred}}(z_i))^2.$ <sup>6</sup> $\sigma_{H(z)}$  usually represents the uncertainty (standard deviation) of H(z) and is used to construct a Gaussian

distribution to describe the statistical properties of the measured value. For example, measurement of H(z)value is generally assume that obey gaussian distribution:  $H_{\text{obs}}(z) \sim \mathcal{N}(H(z), \sigma_{H(z)}^2)$ . In this way, the Gaussian distribution is used to describe the statistical error of the measured value, rather than H(z) itself.

In this work, we consider the physical relationships between the data in order to introduce the covariance matrix and KL divergence of the data. This approach not only allows for model-independent reconstruction but also enhances the analysis of cosmological models by considering the relationships between data, thereby improving the interpretation of their behavior. For the H(z) data, we use the latest OHD in the range including the recent 31 point at  $0.179 \le z \le 1.965$  (Jimenez et al., 2003; Simon et al., 2005; Stern et al., 2010; Moresco et al., 2012, 2015, 2016; Zhang et al., 2014; Ratsimbazafy et al., 2017), and the new point at z = 0.80 (Jiao et al., 2022) <sup>7</sup> and the point at z = 1.26 (Tomasetti et al., 2023). We consider the total covariance matrix, which combines the statistical and systematic errors (Moresco et al., 2020) of 15 H(z) estimates in the range 0.179 < z < 1.965 (Moresco et al., 2012, 2016, 2015). At first, we considered more complexity in the observed data sets by defining a new loss function analogous to the MCMC log-likelihood for the covariance matrix of data (Dialektopoulos et al., 2023), which allows the model to properly account for the data uncertainties.

$$L_{\chi^2} = \sum_{i:j}^{N} \left[ H_{\text{obs}}(z_i) - H_{\text{pred}}(z_i) \right]^{\text{T}} C_{ij}^{-1} \left[ H_{\text{obs}}(z_j) - H_{\text{pred}}(z_j) \right]. \tag{4}$$

Where  $C_{ij}$  is the total covariance matrix of 15  $H(z)^8$ . To further ensure that the model provides high confidence in the probability distribution of the outputs while directly optimizing the deviation between the predicted and true values, we adopted KL divergence combined with the MCMC log-likelihood as the loss function for optimization,

$$\mathcal{L}_{\text{com}} = D_{\text{KL}} + L_{\chi^2}. \tag{5}$$

The degree of complexity of the ANN should reflect the structure of the physical process which is producing the data. In order to obtain optimal ANN model before training with the actual data set, we generate a mock data set  $^9$  to mimics the observed points. For the training procedure, we consider the mock H(z) data set with the number of hidden layers varying from one to three, and eight network models are trained with  $2^n$  number of neurons, where  $7 \le n \le 14$ . The network model for reconstructing H(z) is optimized by using mock H(z) data which has the same number as that of the actual OHD; while the training batch size  $^{10}$  is set to half of the number of the H(z) data points. We calculate the RISK $^{11}$  of eight models for each network structure.

<sup>&</sup>lt;sup>7</sup>More recently, Borghi et al. (2022) explored a new approach to obtain a piont OHD at z = 0.75. Jiao et al. (2022) proposed a similar approach to obtain a point at z = 0.80. For these two measurements are not fully independent and their covariance is not clear, Zhang et al. (2022) only use the point Jiao et al. (2022) with other 31 OHD to calibrate of HII Galaxies.

<sup>8</sup>https://gitlab.com/mmoresco/CCcovariance/-/tree/master?ref\_type=heads

<sup>&</sup>lt;sup>9</sup>Following the method proposed by Ma & Zhang (2011), the simulated data can be given by assuming the spatially-flat  $\Lambda$ CDM model with the simulated redshift distribution subjects to a Gamma distribution for the redshift distribution histogram of the actual OHD. Assuming a linear model for the error of H(z) to fit a first degree polynomial function of redshift, and the Guassian distribution of the error  $\tilde{\sigma}_H(z)$ :  $\mathcal{N}(\sigma_H^0(z), \varepsilon_H(z))$ , where  $\varepsilon_H(z) = (\sigma_H^+(z) - \sigma_H^-(z))/4$ , such that  $\tilde{\sigma}_H(z)$  falls in the area with a probability of 95%. The simulated Hubble parameter data point  $H_{sim}(z_i)$  at redshift  $z_i$  with the associated uncertainty of  $\tilde{\sigma}_H(z_i)$  is computed by  $H_{sim}(z_i) = H_{fid}(z_i) + \Delta H_i$ , where  $\Delta H_i$  is determined via  $\mathcal{N}(0, \tilde{\sigma}_H(z_i))$ .

<sup>&</sup>lt;sup>10</sup>Batch: A small part of the samples in the training set are used to update the parameters of the model weights in a back propagation.

<sup>&</sup>lt;sup>11</sup>Following Wang et al. (2020), we adopt the risk statistic to select the optimal number of hidden layers of the network: RISK =  $\sum_{i=1}^{N} \text{BIAS}_{i}^{2} + \sum_{i=1}^{N} \text{VARIANCE}_{i}$ , where N is the number of H(z) data points,  $\bar{H}(z_{i})$  denotes the fiducial value of H(z).

The initial learning rate is set to 0.01 which will decrease with the number of iterations. The network is trained after  $3 \times 10^5$  iterations, ensuring that the function no longer decreases. We inferred that the network model with one hidden layer minimizes the RISK with respect to the two and three hidden layer training networks. Given that we are using H(z) data alone, the lack of complexity in the data seems to infer a simpler one-layer structure to the ANN. We could clearly observe find that 4096 neurons minimize the risk function. Consequently, the network structure with one hidden layer and 4096 neurons was found to be the optimal network structure and will therefore be adopted in our H(z) reconstructions.

In Fig. 2, we show results of reconstruction for the latest OHD with different loss functions  $(D_{\text{KL}}, L_{\chi^2}, \mathcal{L}_{\text{com}})$ , as well as MSE (one and two ANNs to train  $\sigma_{H(z)}$  and H(z) without accounting for the data uncertainties) respectively. Although the shapes of reconstruction of H(z) are similar, results with the loss function  $\mathcal{L}_{\text{com}}$  exhibits a more accurate and stable reconstruction. This is particularly evident in the regions where the data points are sparse,  $\mathcal{L}_{\text{com}}$  appears capture the underlying trend and minimize fluctuations more accurately. As a result,  $\mathcal{L}_{\text{com}}$  demonstrates superior performance in modeling the Hubble parameter H(z), particularly when compared to the  $D_{\text{KL}}$  and  $L_{\chi^2}$  functions, which do not fully leverage the data's intrinsic relationships.

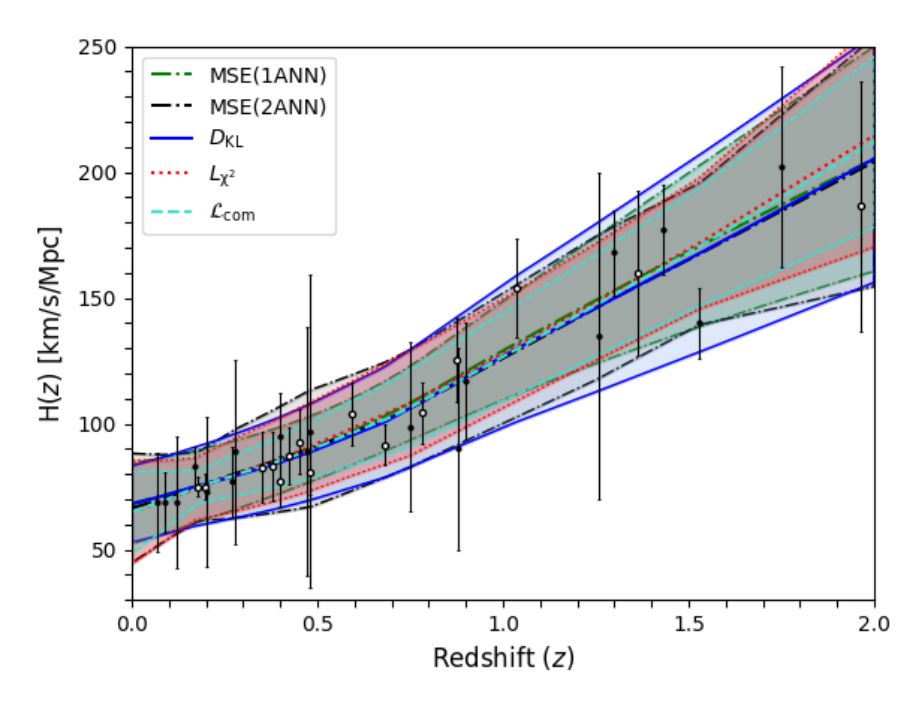


Figure 2: Results of reconstruction used the latest OHD with different loss functions ( $D_{\text{KL}}, L_{\chi^2}$ , and  $\mathcal{L}_{\text{com}}$ ) as well as MSE (one and two ANNs to train  $\sigma_{H(z)}$  and H(z) without accounting for the data uncertainties) respectively. The black cycles and dots indicate the 15 OHD with the full covariance matrices and the other 18 OHD without covariance, respectively. The error represent only the diagonal part of the covariance matrix; the full covariance should be taken into account to use the data appropriately.

### 3. GRB Hubble Diagram

In this paper, we calibrate the Amati relation with A219 GRB data<sup>12</sup> and J220 GRB data<sup>13</sup> at low redshift by reconstructing the Hubble parameter from the latest OHD in ANN framework to build GRB Hubble diagram. For reconstruction, we use the recent 33 point at  $0.179 \le z \le 1.965$  including the new points at z = 0.80 (Jiao et al., 2022) and at z = 1.26 (Tomasetti et al., 2023). Therefore, we use the redshift cutoff at z = 1.965 to calibrate the Amati relation with A219 (115 GRBs) and J220 (128 GRBs) samples. Montiel et al. (2021) calibrated the Amati relation with OHD at z < 1.43, according to the analysis of Moresco et al. (2020) that OHD was carried out through simulations in the redshift range 0 < z < 1.5. In order to compare with the previous analyses (Liang et al., 2022; Liu et al., 2022b; Li, Zhang & Liang, 2023), we also use a subsample including 29 OHD points with a redshift cutoff at z = 1.4 to calibrate the Amati relation with A219 (79 GRBs) and J220 (90 GRBs) samples.

The Amati relation (Amati et al., 2002), which refers to the power-law relationship between the spectral peak energy  $E_{\text{peak}}$  and the isotropic equivalent energy  $E_{\text{iso}}$  of GRBs, can be expressed in the logarithmic form,

$$\log E_{\rm iso} = a + b \cdot \log E_{\rm p} \tag{6}$$

where a and b are free coefficients, and

$$E_{\rm iso} = 4\pi d_L^2(z) S_{\rm bolo}(1+z)^{-1}, \quad E_{\rm p} = E_{\rm p}^{\rm obs}(1+z)$$
 (7)

where  $E_{\rm iso}$  is in units of 1 erg,  $E_{\rm p}^{\rm obs}$  in units of 300keV,  $S_{\rm bolo}$  is the observed value of the bolometric fluence. The values of the Hubble parameter H(z) can be reconstructed by ANN specifically at redshifts of GRBs. For a flat space, the luminosity distance can be calculated,

$$d_L^{\text{ANN}} = c(1+z) \int_0^z \frac{dz'}{H(z')}.$$
 (8)

It is important to note that the likelihood approach by D'Agostini (2005) could introduce subjectivity regarding the selection of the independent variable. The likelihood function proposed by Reichart (2001) which advantageously eliminates the need to arbitrarily designate an independent variable between  $E_p$  and  $E_{\rm iso}$  has been used in (Amati & Della Valle , 2013). The D'Agostini (2005) and Reichart (2001) likelihood functions can be expressed as (Lin et al., 2016; Li, Zhang & Liang, 2023)

$$\mathcal{L}_{D} \propto \prod_{i=1}^{N_{1}} \frac{1}{\sigma_{D}} \times \exp\left[-\frac{[y_{i} - y(x_{i}, z_{i}; a, b)]^{2}}{2\sigma_{D}^{2}}\right], \tag{9}$$

here  $\sigma_{\rm D} = \sqrt{\sigma_{\rm int,D}^2 + \sigma_{y_i}^2 + b^2 \sigma_{x_i}^2}$ , the intrinsic scatter  $\sigma_{\rm int,D}$  which represents any other unknown errors except for the measurement error can be treated as a free parameter.

$$\mathcal{L}_{R} \propto \prod_{i=1}^{N_1} \frac{\sqrt{1+b^2}}{\sigma_{R}} \times \exp\left[-\frac{[y_i - y(x_i, z_i; a, b)]^2}{2\sigma_{R}^2}\right]. \tag{10}$$

<sup>&</sup>lt;sup>12</sup>Following Liang et al. (2022), we excluded GRB051109A from the A220 sample, which incorporates the A118 dataset with the lowest intrinsic dispersion, along with the A102 dataset from the 193 GRBs analyzed by Amati et al. (2019) and Demianski et al. (2017).

<sup>&</sup>lt;sup>13</sup>Following Khadka et al. (2021) and Cao & Ratra (2024), we have removed GRB020127 which has an unreliable redshift from the J221 GRB sample (Jia et al., 2022).

Table 1: Calibration results (the intercept a, the slope b, and the intrinsic scatter  $\sigma_{\rm int}$ ) with the Amati relation for the A219 and J220 samples at  $z \le 1.965$  and  $z \le 1.4$ .

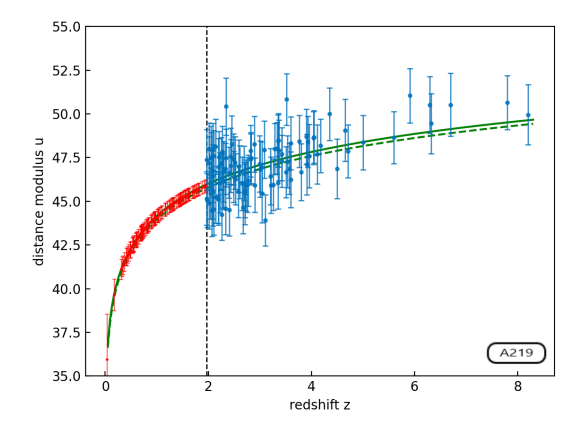
Sample	Methods	a	b	$\sigma_{ m int,D}/\sigma_{ m int,R}$
A219 (115 GRBs at $z \le 1.965$ )	D'Agostini	$52.79^{+0.05}_{-0.05}$	$1.34^{+0.10}_{-0.10}$	$0.52^{+0.03}_{-0.04}$
	Reichart	$52.77^{+0.06}_{-0.06}$	$1.90^{+0.01}_{-0.03}$	$0.58^{+0.04}_{-0.05}$
J220 (128 GRBs at $z \le 1.965$ )	D'Agostini	$52.84^{+0.04}_{-0.04}$	$1.52^{+0.08}_{-0.08}$	$0.42^{+0.03}_{-0.03}$
	Reichart	$52.83^{+0.04}_{-0.04}$	$1.90^{+0.09}_{-0.03}$	$0.45^{+0.03}_{-0.04}$
A219 (79 GRBs at $z \le 1.4$ )	D'Agostini	$52.73^{+0.06}_{-0.06}$	$1.28^{+0.13}_{-0.13}$	$0.53^{+0.04}_{-0.05}$
	Reichart	$52.75^{+0.07}_{-0.07}$	$1.86^{+0.13}_{-0.05}$	$0.59^{+0.05}_{-0.06}$
J220 (90 GRBs at $z \le 1.4$ )	D'Agostini	$52.80^{+0.05}_{-0.05}$	$1.57^{+0.09}_{-0.09}$	$0.41^{+0.03}_{-0.04}$
	Reichart	$52.81_{-0.05}^{+0.05}$	$1.89_{-0.03}^{+0.11}$	$0.43^{+0.15}_{-0.08}$

here  $\sigma_{\rm R} = \sqrt{\sigma_{\rm int,R}^2 + \sigma_{y_i}^2 + b^2 \sigma_{x_i}^2}$ ,  $\sigma_{\rm int,R}$  can be calculated by the "equivalent" total intrinsic scatter (Lin et al., 2016):  $\sigma_{\rm equi} = \sqrt{\sigma_{y,\rm ext}^2 + b^2 \sigma_{x,\rm ext}^2}$ , in which  $\sigma_{x,\rm ext}$  and  $\sigma_{y,\rm ext}$  are the extrinsic scatter along the x-axis and y-axis (Reichart, 2001). In this work, we treat the total intrinsic scatter  $\sigma_{\rm int,R}$  as a free parameter.

We employ the Markov Chain Monte Carlo (MCMC) method, facilitated by the Python package emcee (Foreman-Mackey et al., 2013), which refines the Metropolis-Hastings algorithm. The calibration outcomes, encompassing the intercept a, the slope b, and the intrinsic scatter  $\sigma_{\rm int}$ , for the A219 and J220 samples at  $z \leq 1.965$  and  $z \leq 1.4$  are detailed in Table 1. We find that the values of the intercept (a) by the two likelihood function methods are consistent in  $1\sigma$ uncertainty; and the values of slope (b) by Reichart (2001) method are close to the typical value  $(b=2, E_{\rm iso} \propto E_{\rm p}^2)$ ; the value of the intrinsic scatter of the Reichart (2001) method calculated by the fitting values of  $\sigma_{y,\text{int}}$  and  $\sigma_{x,\text{int}}$  are smaller than the total intrinsic scatter  $\sigma_{\text{int,R}}$  treated as a free parameter, which indicate that there are possible systematic errors in fitting procedure. We also find the calibration results with the GRB samples at  $z \leq 1.965$  are consistent with the GRB samples at  $z \leq 1.4$ . For the A219 sample at z < 1.4, we find the fitting value of slope (b =  $1.28^{+0.13}_{-0.13}$ ) by D'Agostini (2005) method align with prior analyses which based on SNe Ia at z < 1.4 utilized GaPP:  $1.298^{+0.090}_{-0.080}$  (Liang et al., 2022) and interpolation:  $1.290^{+0.126}_{-0.126}$  (Liu et al., 2022b). For the J220 sample <sup>14</sup> at z < 1.4 our result ( $b = 1.57^{+0.09}_{-0.09}$ ) is consistent with that of the fourth sub-sample ( $1.35 \le z < 1.49$ ) in Jia et al. (2022):  $1.51^{+0.17}_{-0.17}$  and that by GaPP:  $1.59^{+0.10}_{-0.10}$  (Xie et al., 2024), which is different with Cao & Ratra (2024) by the simultaneous fitting for the  $\Lambda$ CDM model: 1.171 $^{+0.087}_{-0.087}$ . It is worth noting that for the values of  $\sigma_{\rm int}$  obtained with the J220 sample are smaller than ones obtained with the A219 sample; and the values of  $\sigma_{\rm int}$  obtained by the D'Agostini (2005) method are smaller than ones obtained by the Reichart (2001) method.

To ensure objectivity in selecting the independent variable, we choose to use the calibration results by Reichart's likelihood method to construct the GRB Hubble diagram. Assuming that the calibration results of the Amati relation at  $z \le 1.965$  are still applicable at higher redshifts, we can deduce the luminosity distances of GRBs at z > 1.965. The Hubble diagram for GRBs

 $<sup>^{14}</sup>$ Jia et al. (2022) utilized the standard cosmological parameters from Plank Collaboration (2020) ( $\Omega_{\rm m}=0.315,\,\Omega_{\Lambda}=0.685,\,{\rm and}\,\,H_0=67.4\,{\rm km}\,\,s^{-1}\,{\rm Mpc}^{-1}$ ) without any error to obtain the values of  $E_{\rm iso}$ . Cao & Ratra (2024) used the updated values for 7 GRBs from Dirirsa et al. (2019) by simultaneously constraining. Here we use the original values fitted with the Band model (Jia et al., 2022) in J220 GRB sample.



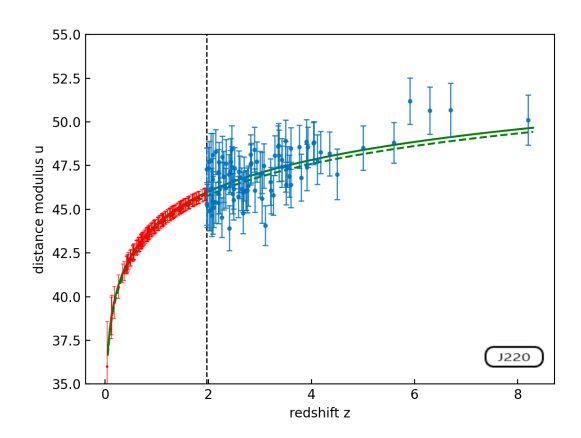


Figure 3: The Hubble diagram of GRBs is presented with the A219 (left) and J220 (right) samples. GRBs data at  $z \leq 1.965$  (red points) were obtained from the OHD data using ANN, GRBs data at z > 1.965 (blue points) are derived from the Amati relation. The solid curve and the dotted curve represent the standard distance modulus fitting from CMB:  $H_0 = 67.36$  km  $s^{-1}$  Mpc<sup>-1</sup>,  $\Omega_m = 0.315$  (Plank Collaboration, 2020), and Pantheon+:  $H_0 = 73.6$  km  $s^{-1}$  Mpc<sup>-1</sup>,  $\Omega_m = 0.334$  (Brout et al., 2022), respectively.

is illustrated in Figure 3. The uncertainty in the GRB distance modulus is

$$\sigma_{\mu}^{2} = \left(\frac{5}{2}\sigma_{\log \frac{E_{\rm iso}}{1 \text{erg}}}\right)^{2} + \left(\frac{5}{2 \ln 10} \frac{\sigma_{S_{\rm bolo}}}{S_{\rm bolo}}\right)^{2} \tag{11}$$

where  $\sigma_{\log \frac{E_{\rm iso}}{\rm lerg}}^2 = \sigma_{\rm int}^2 + (\frac{b}{\ln 10} \frac{\sigma_{E_p}}{E_p})^2 + \sum_{i=1}^{\infty} \left(\frac{\partial_y(x;\theta_c)}{\partial \theta_{c_i}}\right)^2 C_{ii}$ , here  $\theta_c = \sigma_{\rm int}, a, b$ , and  $C_{ii}$  means the diagonal element of the covariance matrix of these fitting coefficients.

# 4. Constraints on DE Models

In order to constrain cosmological models, we use the GRB data in the Hubble diagram at z > 1.4 with the Pantheon+ sample (Scolnic et al., 2022), which consists of 1701 light curves of 1550 unique spectroscopically confirmed SNe Ia at the redshift range 0.001 < z < 2.26 with the observed distance modulus of SNe given by

$$\mu_{\rm SN} = m_{\rm B,corr}^* - M_{\rm B},\tag{12}$$

where  $m_{\mathrm{B,corr}}^* = m_{\mathrm{B}}^* + \alpha X_1 - \beta \mathcal{C} + \Delta_M + \Delta_B$ ,  $m_{\mathrm{B}}^*$  is the observed peak magnitude in rest frame B-band,  $X_1$  is the time stretching of the light-curve,  $\mathcal{C}$  is the SNe color at maximum brightness;  $\alpha$ ,  $\beta$  are nuisance parameters which should be fitted simultaneously with the cosmological parameters,  $\Delta_M$ ,  $\Delta_B$  are the distance correction based on the host galaxy mass of the SN and distance correction based on predicted biases from simulations, respectively;  $M_{\mathrm{B}}$  is the absolute magnitude which can be calibrated by setting an absolute distance scale with primary distance anchors such as Cepheids. The SH0ES (Supernovae and  $H_0$  for the Equation of State of dark energy) team obtained  $M_B = -19.253 \pm 0.027$  (Riess et al., 2022) from the Pantheon+sample (Scolnic et al., 2022; Brout et al., 2022). In this work, we set  $M_{\mathrm{B}} = -19.253$  (Riess et al., 2022) for simplicity. Liu et al. (2022b) used  $M_{\mathrm{B}} = -19.36$  with the Pantheon sample, BAO, and CC (Gomez-Valent, 2022) to calibrate the Amati relation and the improved Amati relation. Mukherjee et al. (2024a) employed neural networks to obtain:  $M_{\mathrm{B}} = -19.353^{+0.073}_{-0.078}$  from the Pantheon+ and CC sample. Mukherjee et al. (2024b) calibrated the Dainotti relations by setting  $M_{\mathrm{B}} = -19.35$  for simplicity. In order to investigate the influence for the

value of  $M_{\rm B}$  in the subsequent constraints, we also use  $M_{\rm B}=-19.353~(\Delta M_B\approx 0.10)$  for comparison. It should be noted that  $M_{\rm B}$  can be also treated as a free parameter in fitting procedure (Liang et al., 2022; Li, Zhang & Liang, 2023); and we can also treat  $M_{\rm B}-\mu_0$  (where  $\mu_0=5\log h-42.38,~h=H_0/(100{\rm km/s/Mpc}),~H_0$  is the Hubble constant) as a free parameter, which can be marginalized over analytically to avoid the degeneracy between  $M_B$  and  $H_0$  (Li et al., 2020).

The  $\chi^2$  for the distance modulus can be expressed as

$$\chi_{\mu}^{2} = \sum_{i=1}^{N} \left[ \frac{\mu_{\text{obs}}(z_{i}) - \mu_{\text{th}}(z_{i}; p, H_{0})}{\sigma_{\mu_{i}}} \right]^{2}.$$
 (13)

Here  $\mu_{\text{obs}}$  is the observational value of distance modulus and its error  $\sigma_{\mu_i}$ , and  $\mu_{\text{th}}$  is the theoretical value of distance modulus calculated from the cosmological parameters p,

$$\mu_{\rm th} = 5 \log \frac{d_L}{\text{Mpc}} + 25 = 5 \log D_L - \mu_0,$$
 (14)

For a flat space, the unanchored luminosity distance  $D_L$  can be calculated by  $D_L \equiv \frac{H_0 d_L}{c} = (1+z) \int_0^z \frac{dz'}{E(z')}$ , where c is the light speed,  $E(z) = [\Omega_{\rm M}(1+z)^3 + \Omega_{\rm DE}X(z)]^{1/2}$ , and  $X(z) = \exp[3\int_0^z \frac{1+w(z')}{1+z'}dz']$ , which is determined by the choice of DE model.

BAOs offer a distinct perspective on the universe's structure and evolution, which can be used as an invaluable tool for probing cosmological models at mid-redshift. In order to tighten the constraints on cosmological parameters, we combine GRBs and SNe with BAOs.<sup>15</sup> The likelihood of BAO can be expressed as,

$$\chi^2_{\rm BAO} = \Delta P_{\rm BAO} C_{\rm BAO}^{-1} \Delta P_{\rm BAO}^{\rm T},$$

where  $\Delta P_{\rm BAO} = v_{\rm obs}(z) - v_{\rm th}(z)$ ,  $v_{\rm obs}(z)$  is a BAO measurement <sup>16</sup> of the observed points at each z, and  $v_{\rm th}(z)$  is the prediction of the theoretical model,  $C_{\rm BAO}$  is the covariance matrix of the observed points. Here we use BAO data including the 6dF Galaxy Survey (6dFGS) at  $z_{\rm eff} = 0.106$ , the Sloan Digital Sky Survey (SDSS) DR7 Main Galaxy Sample (MGS) at  $z_{\rm eff} = 0.15$ , and nine measurements from the extended Baryon Oscillation Spectroscopic Survey (eBOSS) DR16 at  $z_{\rm eff} = 0.38, 0.51, 0.70, 0.85, 1.48$  (Wang, Li & Liang, 2024). We also consider the latest BAO measurements  $(D_{\rm H}(z)/r_{\rm d}, D_{\rm M}(z)/r_{\rm d})$  and  $D_{\rm V}(z)/r_{\rm d} = \frac{1}{r_{\rm d}} [\frac{cz}{H(z)}]^{1/3} [\frac{D_{\rm L}}{1+z}]^{2/3})$  from Dark Energy Spectroscopy Instrument (DESI) at  $z_{\rm eff} = 0.295, 0.510, 0.706, 0.930, 1.317, 1.491, 2.330$  (DESI Collaboration, 2024).

The total  $\chi^2$  with the joint data of GRB+SNe and BAO can be expressed as  $\chi^2_{\text{total}} = \chi^2_{\text{GRB}} + \chi^2_{\text{SN}} + \chi^2_{\text{BAO}}$ . The python package *emcee* by the MCMC method (Foreman-Mackey et al., 2013) is used to constrain DE models. We consider three DE models in a flat space, the  $\Lambda$ CDM model with dark energy EoS w = -1, the wCDM model with a constant Equation of State (EoS), and the Chevallier-Polarski-Linder (CPL) model (Chevallier & Polarski, 2001; Linder, 2003) in which DE evolving with redshift as a parametrization EoS,  $w = w_0 + w_a z/(1+z)$ .

<sup>&</sup>lt;sup>15</sup>It should be noted that BAO measurements which under a fiducial cosmology could provide biased constraints.

 $<sup>^{16}</sup>$  The BAO feature appears in both the line-of-sight direction and the transverse direction and provides measurements of the radial projection:  $\frac{D_{\rm H}(z)}{r_{\rm d}} = \frac{c}{H(z)r_{\rm d}}$  and the transverse comoving distance  $\frac{D_{\rm M}(z)}{r_{\rm d}} = \frac{c}{H_0r_{\rm d}}\Gamma(z)$ , where  $\Gamma(z) = \int_0^z dz'/E(z')$  in a flat space, the sound horizon is defined as  $r_{\rm d} = \frac{c}{H_0} \int_{z_d}^{\infty} \frac{c_{\rm s}}{E(z')dz'}$  at the drag epoch  $z_{\rm d}$ . We use the constrained value from Plank Collaboration (2020) ( $r_{\rm d} = 147.05 \pm 0.30 {\rm Mpc}, z_d = 1089.80 \pm 0.21$ ).  $r_{\rm d}$  can be also treated as a free parameter (Li et al., 2020).

The angular diameter distance  $D_{\rm A}(z)$  has relation with  $D_{\rm M}(z)$ :  $D_{\rm A}(z) = D_{\rm M}(z)/(1+z)$ .

Table 2: Constraints on parameters of  $\Omega_m$ , h,  $w_0$  and  $w_a$  for the flat  $\Lambda$ CDM model, the flat wCDM model, and the flat CPL model only with the A219 and J220 samples (z > 1.965).

Models	Data Set	$\Omega_m$	h	$w_0$	$w_a$	$\Delta { m AIC}$	$\Delta \mathrm{BIC}$
$\Lambda \text{CDM}$	A219	$0.377^{+0.071}_{-0.17}$	$0.629^{+0.056}_{-0.082}$	-	-	0	0
$w\mathrm{CDM}$	A219	$0.380^{+0.11}_{-0.17}$	$0.620^{+0.041}_{-0.11}$	$-1.09^{+0.58}_{-0.76}$	-	1.82	4.46
CPL	A219	$0.382^{+0.070}_{-0.17}$	$0.630^{+0.051}_{-0.10}$	$-1.02^{+0.55}_{-0.55}$	$-1.01^{+0.58}_{-0.58}$	3.58	8.87
$\Lambda \mathrm{CDM}$	J220	$0.379^{+0.072}_{-0.17}$	$0.633^{+0.059}_{-0.080}$	-	-	0	0
$w\mathrm{CDM}$	J220	$0.380^{+0.084}_{-0.17}$	$0.621^{+0.044}_{-0.11}$	$-1.08^{+0.51}_{-0.51}$	-	1.78	4.30
CPL	J220	$0.386^{+0.076}_{-0.17}$	$0.628^{+0.045}_{-0.10}$	$-0.96^{+0.88}_{-0.37}$	$-1.03^{+0.58}_{-0.58}$	3.44	8.49

Constraints only with A219 and J220 samples at z > 1.965 are summarized in Table 2. For the  $\Lambda$ CDM model, we obtain  $\Omega_{\rm m} = 0.377^{+0.071}_{-0.17}$ ,  $h = 0.629^{+0.065}_{-0.082}$ , with the A219 sample, and  $\Omega_{\rm m} = 0.379^{+0.072}_{-0.17}$ ,  $h = 0.633^{+0.059}_{-0.080}$ , with the J220 sample at the  $1\sigma$  confidence level, respectively. There is evident that the  $\Lambda$ CDM model ( $w_0 = -1$ ,  $w_a = 0$ ) remains the best-fit to the observational data according to the results of the wCDM model and the CPL model. We find the results using GRBs alone with the A219 sample are consistent with the J220 sample, which are compatible with the previous works of Li, Zhang & Liang (2023).

Joint constraints combining GRBs with the A219 and J220 (right) ( $z \ge 1.965$ ) and SNe, BAOs are shown in Fig. 4 ( $\Lambda$ CDM), Fig. 5 (wCDM) and Fig. 6 (CPL), which are summarized in Table 3. Combining SNe Ia and BAOs with GRB samples, we find the results are consistent with the A219 and J220 samples. For the  $\Lambda$ CDM model, we obtain  $\Omega_{\rm m} = 0.382^{+0.021}_{-0.024}$ ,  $h = 0.7248 \pm 0.0030$  and  $\Omega_{\rm m} = 0.380 \pm 0.022$ ,  $h = 0.7250 \pm 0.0031$  with A219+SNe+SDSS and J220+SNe+SDSS at the  $1\sigma$  confidence level, respectively; as well as  $\Omega_{\rm m} = 0.335^{+0.011}_{-0.013}$ ,  $h = 0.7298 \pm 0.0022$  and  $\Omega_{\rm m} = 0.334 \pm 0.012$ ,  $h = 0.7298 \pm 0.0022$  with A219+SNe+DESI and J220+SNe+DESI at the  $1\sigma$  confidence level, respectively. We find there is evident that the results of the wCDM model  $w_0 \neq -1$  and the CPL model somewhat support EoS ( $w_0 > -1$ ) variations with redshift ( $w_a \neq 0$ ). We also find the constraint results with the GRB samples at z > 1.965 are consistent with the GRB samples at z > 1.4.

 $H_0$  with a redshift evolving is an interesting idea (Dainotti et al., 2021, 2025) for the well-known  $H_0$  tension (Hu & Wang, 2023). We compare to the fitting results from CMB data based on the  $\Lambda$ CDM model at very high-redshift ( $H_0 = 67.36 \text{ km s}^{-1} \text{ Mpc}^{-1}$ ,  $\Omega_m = 0.315$ )(Plank Collaboration, 2020) and SNe Ia at very low-redshift ( $H_0 = 74.3 \text{ km s}^{-1} \text{ Mpc}^{-1}$ ,  $\Omega_m = 0.298$ )(Scolnic et al., 2022). Because of the degeneracy between  $M_B$  and  $H_0$ , a high  $M_B$  inherently leads to a higher  $H_0$ . For example,  $\Delta M_B \approx 0.10$  correspond to  $\Delta H_0 \approx 3.0$ . Adding BAO at relative low redshift to joint constraints will also contributes to a higher  $H_0$ . We also find  $\Omega_{\rm m} \approx 0.40$  for the  $\Lambda$ CDM model with GRBs at relative high redshift, while adding BAO at relative low redshift will remove this trend (Wang, Li & Liang, 2024).

Finally, we compare the dark energy models using the Akaike Information Criterion (AIC) and Bayesian Information Criterion (BIC), which are defined as follows:AIC =  $-2 \ln \mathcal{L}_{\text{max}} + 2k$ , BIC =  $-2 \ln \mathcal{L}_{\text{max}} + k \ln N$ . where  $\mathcal{L}_{\text{max}}$  represents the maximum likelihood. For the Gaussian case,  $\chi^2_{\text{min}} = -2 \ln \mathcal{L}_{\text{max}}$ . The results for the values of  $\Delta$ AIC and  $\Delta$ BIC relative to the reference model (the  $\Lambda$ CDM model) are summarized in Table 3. We find that the  $\Lambda$ CDM model is preferred over the wCDM and CPL models, which is consistent with previous analyses (Amati et al., 2019; Montiel et al., 2021; Li, Zhang & Liang, 2023; Wang, Li & Liang, 2024;

Table 3: Joint constraints on parameters of  $\Omega_m$ , h,  $w_0$  and  $w_a$  for the flat  $\Lambda$ CDM model, the flat wCDM model, and the flat CPL model combining GRBs with the A219 and J220 samples (z > 1.965) with SNe, and BAOs (SDSS and DESI).

Models	Data Set	$\Omega_m$	h	$w_0$	$w_a$	$\Delta { m AIC}$	$\Delta \mathrm{BIC}$
$\Lambda$ CDM	A219+SNe+SDSS	$0.382^{+0.021}_{-0.024}$	$0.7248 \pm 0.0030$	-	-	0	0
	$A219{+}SNe{+}DESI$	$0.335^{+0.011}_{-0.013}$	$0.7298 \pm 0.0022$	-	-	0	0
	$\rm J220{+}SNe{+}SDSS$	$0.380^{+0.022}_{-0.022}$	$0.7250 \pm 0.0031$	-	-	0	0
	J220+SNe+DESI	$0.334^{+0.012}_{-0.012}$	$0.7298 \pm 0.0022$	-	-	0	0
wCDM	A219 + SNe + SDSS	$0.345^{+0.028}_{-0.033}$	$0.7231 \pm 0.0027$	$-0.90^{+0.08}_{-0.05}$	-	2.85	8.35
	$A219{+}SNe{+}DESI$	$0.313^{+0.011}_{-0.013}$	$0.7250 \pm 0.0023$	$-0.87^{+0.03}_{-0.02}$	-	3.37	8.87
	$\rm J220{+}SNe{+}SDSS$	$0.339^{+0.026}_{-0.031}$	$0.7232 \pm 0.0027$	$-0.88^{+0.07}_{-0.05}$	-	2.66	8.16
	$\rm J220{+}SNe{+}DESI$	$0.311^{+0.012}_{-0.012}$	$0.7252 \pm 0.0024$	$-0.87^{+0.03}_{-0.02}$	-	3.34	8.86
CPL	$A219{+}SNe{+}SDSS$	$0.366^{+0.027}_{-0.030}$	$0.7200 \pm 0.0029$	$-0.75^{+0.10}_{-0.07}$	$-1.46^{+0.18}_{-0.52}$	3.44	14.45
	$A219{+}SNe{+}DESI$	$0.316^{+0.013}_{-0.015}$	$0.7179 \pm 0.0027$	$-0.61^{+0.07}_{-0.05}$	$-1.59^{+0.14}_{-0.36}$	4.21	15.22
	$\rm J220{+}SNe{+}SDSS$	$0.361^{+0.029}_{-0.029}$	$0.7194 \pm 0.0029$	$-0.73^{+0.10}_{-0.07}$	$-1.51^{+0.16}_{-0.48}$	3.21	14.20
	J220+SNe+DESI	$0.318^{+0.013}_{-0.013}$	$0.7177 \pm 0.0027$	$-0.61^{+0.07}_{-0.05}$	$-1.60^{+0.13}_{-0.37}$	4.01	15.03

Wang & Liang, 2024) and (Cao & Ratra, 2024; Jia et al., 2022).

#### 5. Conclusions

Throughout this work, we utilize the latest OHD data to reconstruct H(z) through ANN to calibrate the Amati relation at low redshift with the A219 and J220 samples to construct the GRB Hubble diagram. We consider the physical relationships between the data to introduce the covariance matrix and KL divergence of the data. We find the results are consistent with the A219 and J220 samples combining SNe Ia and BAOs (SDSS or DESI). For the  $\Lambda$ CDM model, we obtain  $\Omega_{\rm m}=0.382^{+0.021}_{-0.024},\ h=0.7248\pm0.0030$  and  $\Omega_{\rm m}=0.335^{+0.011}_{-0.013},\ h=0.7298\pm0.0022$  with A219+SNe+SDSS and A219+SNe+DESI; as well as  $\Omega_{\rm m}=0.380\pm0.022,\ h=0.7250\pm0.0031$  and  $\Omega_{\rm m}=0.334\pm0.012,\ h=0.7298\pm0.0022$  with J220+SNe+SDSS and J220+SNe+DESI at the  $1\sigma$  confidence level, respectively. We find there is evident that the results of the wCDM and CPL models somewhat support EoS ( $w_0>-1$ ) variations with redshift ( $w_a\neq0$ ). Adding BAO at relative low redshift to joint constraints will contributes to a higher  $H_0$ . However, the  $\Lambda$ CDM model is preferred over the wCDM and CPL models using the AIC and BIC.

More recently, Wang & Liang (2024) presented a sample of long GRBs from 15 years of the Fermi-GBM catalogue with identified redshift, in which the GOLD sample contains 123 long GRBs at  $z \leq 5.6$  and the FULL sample contains 151 long GRBs with redshifts at  $z \leq 8.2$ . Jiang et al. (2024) find new features by replacing the Pantheon+ with the Union3 (Rubin et al., 2024) and the full five years of the Dark Energy Survey (DES) Supernova Program (Abbott et al., 2024) to reconstruct the late-time expansion history in light of the latest BAO measurements from DESI (DESI Collaboration, 2024) based on Gaussian processes. Alfano et al. (2024a,b) consider DESI 2024 data to constrain dark energy models with the Amati relation, Yonetoku relation (Yonetoku et al., 2004) and the Combo relation (Izzo et al., 2015) by the

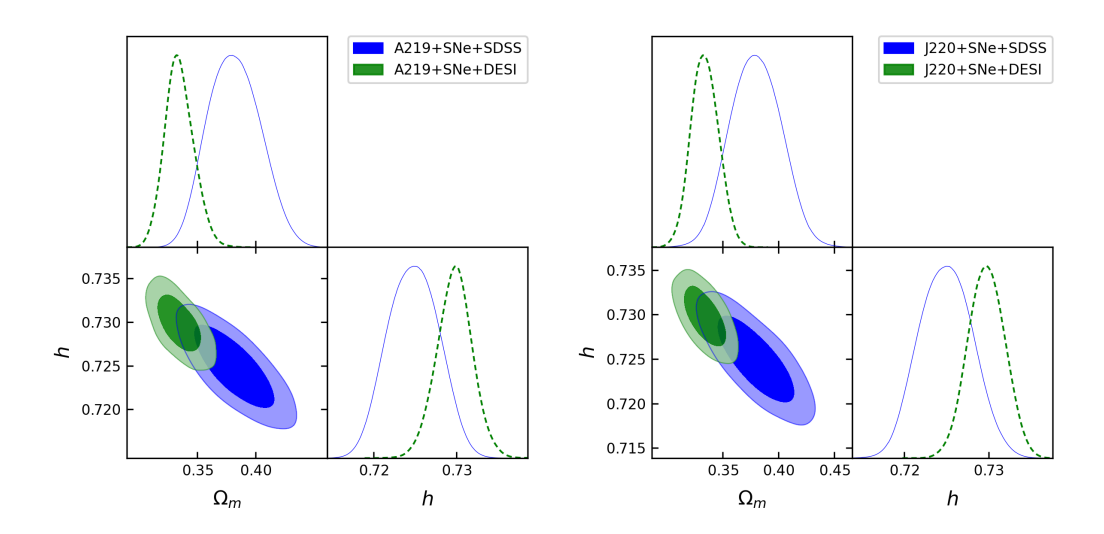


Figure 4: Joint constraints on parameters of  $\Omega_m$ , h for the flat  $\Lambda$ CDM model combining the A219 (left) and J220 (right) samples (z > 1.965) with SNe and BAOs (SDSS and DESI).

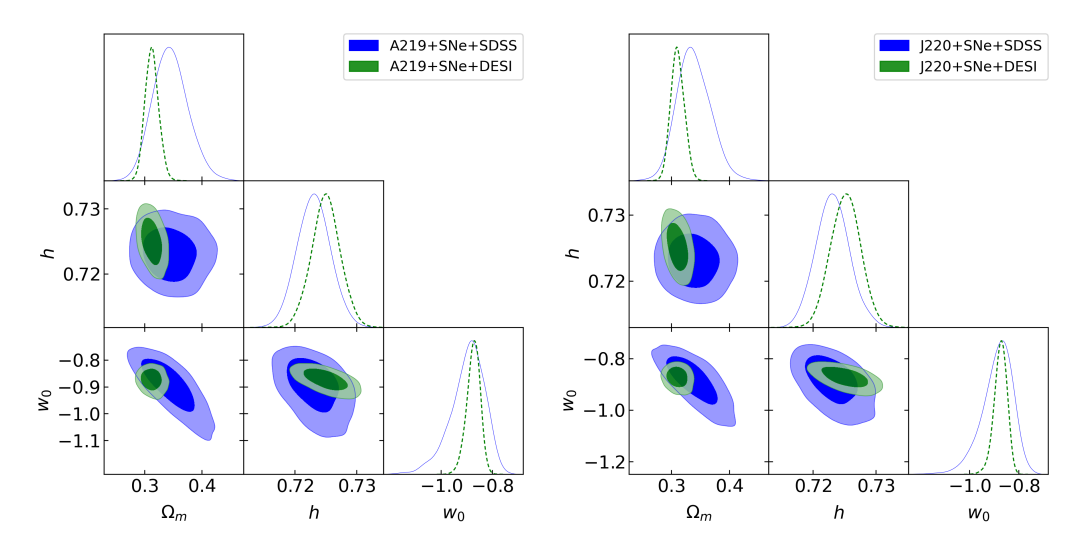


Figure 5: Joint constraints on parameters of  $\Omega_m$ , h, and  $w_0$  for the flat wCDM model combining the A219 (left) and J220 (right) samples (z > 1.965) with SNe and BAOs (SDSS and DESI).

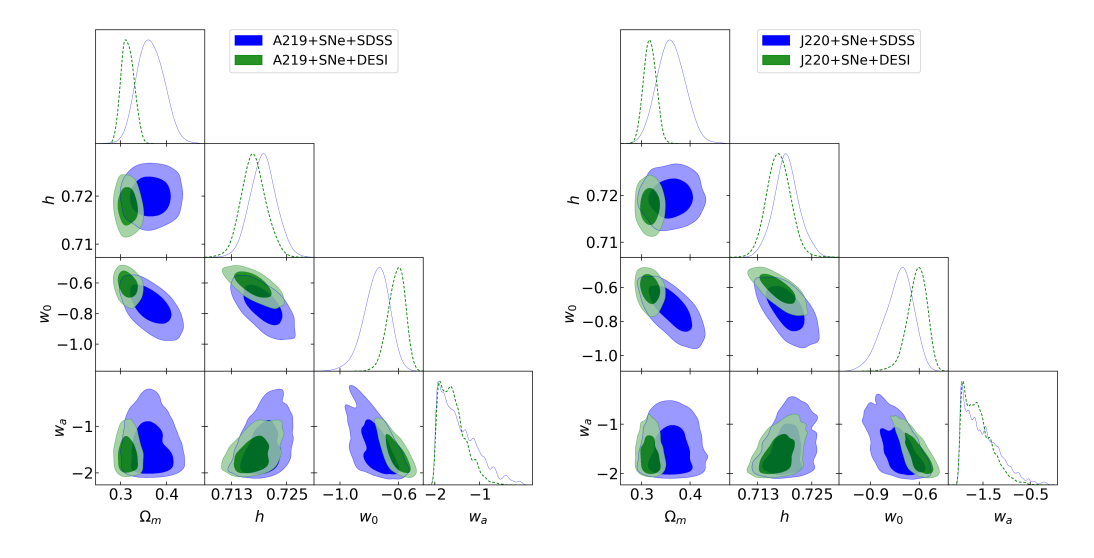


Figure 6: Joint constraints on parameters of  $\Omega_m$ , h,  $w_0$  and  $w_a$  for the flat CPL model combining the A219 (*left*) and J220 (*right*) samples (z > 1.965) with SNe and BAOs (SDSS and DESI).

Bézier parametric approach; as well as the Dainotti relations (Dainotti et al., 2008, 2016, 2020) as standard candles can also be calibrated model-independently (Favalei et al., 2024; Alfano et al., 2024c; Sethi et al., 2024; Zhang et al., 2025; Mukherjee et al., 2024b). In the following work, we expect that adding the 15 years of the Fermi-GBM catalogue at  $0.0785 \le z \le 8.2$ , the SNe Ia from the Union3 sample with 2087 SNe Ia at 0.01 < z < 2.26 and the 5-year DES with 1635 SNe Ia at 0.1 < z < 1.3, as well as BAO measurements from DESI data release will lead to more accurate constraints on the cosmological parameters and the evolutionary behavior of DE.

# Acknowledgments

We thank Yang Liu, Prof. Puxun Wu, Prof. Jianchao Feng for kind help and discussions. We also thank the anonymous referee for helpful comments and constructive suggestions. This project was supported by the Guizhou Provincial Science and Technology Foundation: QKHJC-ZK[2021] Key 020 and QKHJC-ZK[2024] general 443. Y. Liu was supported by the NSFC under Grant No. 12373063.

#### References

Abbott, T. M. C. et al. 2024, ApJL, 973, L1

Alfano, A.C., Luongo, O., Muccino, M. 2024a, JCAP, 12, 055

Alfano, A.C., Luongo, O., Muccino, M. 2024b, arXiv:2411.04878

Alfano, A.C., Luongo, O., Muccino, M. 2024c, JHEAP, 42, 178

Amati, L., D'Agostino, R., Luongo, O., Muccino, M., & Tantalo, M. 2019, MNRAS, 486, L46

Amati, L., Frontera, F., Tavani, M., et al. 2002, A&A, 390, 81

Amati, L., Guidorzi, C., Frontera, F., et al. 2008, MNRAS, 391, 577

Amati, L. & Della Valle 2013, IJMPD, 22, 1330028

Bargiacchi, G., Dainotti, M. G., & Hernandez, X. 2025, New Astronomy Reviews, 100, 101712

Borghi, N., Moresco, M. & Cimatti, A. 2022, ApJL, 928, L4

Brout D., et al., 2022, ApJ, 938, 110

Cao, S., Dainotti, M., & Ratra, B. 2022a, MNRAS, 512, 439

Cao, S., Dainotti, M. G., & Ratra, B. 2022b, MNRAS, 516, 1386

Cao, S. & Ratra, B. 2024, JCAP, 10, 093

Capozziello, S., & Izzo, L. 2008, A&A, 490, 31

Capozziello, S. & Izzo, L. 2009, NuPhS, 194, 206

Capozziello, S., & Izzo, L. 2010, A&A, 519, A73

Cardone, V. F., Capozziello, S., & Dainotti, M. G., 2009, MNRAS, 400, 775

Chen, J. F., Zhang, T. T., Zhang, T-J., & Gai., N. 2024, arXiv: 2410.08369

Chevallier, M. & Polarski, D. 2001, IJMPD, 10, 213

Clevert, Unterthiner, & Hochreiter 2015, arXiv:1511.07289

Cucchiara, A., Levan, A., Fox, D. B., et al. 2011, ApJ, 736, 7

D'Agostini, G. 2005, arXiv: physics/0511182

Dainotti, M. G., Cardone V. F., & Capozziello S. 2008, MNRAS, 391, L79

Dainotti, M. G., Postnikov, S., & Hernandez, X. 2016, ApJ, 825, L20

Dainotti, M. G., & Amati, L., 2018, PASP, 130, 051001

Dainotti, M. G., et al. 2020, ApJ, 904, 97

Dainotti M. G., De Simone B., Schiavone T., et al., 2021, ApJ, 912, 150

Dainotti M. G., et al., 2025, arXiv:2501.11772

Dai, Z., Liang, E., & Xu, D. 2004, ApJ, 612, L101

Dai, Y., Zheng, X.-G., Li, Z. X., et al. 2021, A&A, 651, L8

Demianski, M., Piedipalumbo, E., Sawant, D., & Amati, L. 2017, A&A, 598, A112

Demianski, M., Piedipalumbo, E., Sawant, D., & Amati, L. 2021, MNRAS, 506, 903

DESI Collaboration, Adame, A. G., Aguilar, J., Ahlen, S. et al., arXiv:2404.03002

Dialektopoulos, K., Said, J. L., Mifsud, J., Sultana, J., & Adami, K. Z. 2022, JCAP, 02, 023

Dialektopoulos, K., Mukherjeeb, P., Said, J. L., & Mifsud, J., 2023, EPJC, 83, 956

Dirirsa, F. F., Razzaque, S., Piron, F., et al. 2019, ApJ, 887, 13

Escamilla-Rivera, C., Quintero, M. A. C., & Capozziello, S. 2020, JCAP, 03, 008

Escamilla-Rivera, C., Carvajal M., Zamora C., & Hendry M. 2022, JCAP, 04, 016

Favale, A., Dainotti, M. G., Gómez-Valent, A., & Migliaccio, M. 2024, JHEAp, 44, 323

Foreman-Mackey, D., Hogg, D. W., Lang, D., & Goodman, J. 2013, PASP, 125, 306

Gao, H., Liang, N., & Zhu, Z.-H. 2012, IJMPD, 21, 1250016

Ghirlanda, G., Ghisellini, G., & Lazzati, D. 2004a, ApJ, 616, 331

Ghirlanda, G., Ghisellini, G., Lazzati, D., & Firmani, C. 2004b, ApJ, 613, L13

Ghirlanda, G., Ghisellini, G., & Firmani, C. 2006, New, J. Phys., 8, 123

Gomez-Valent, A. 2022, PhRvD, 105, 043528

Gómez-Vargas I., Medel-Esquivel R., García-Salcedo R., Vázquez J. A. 2023, EPJC, 83, 304

Han, Y., Gao, J., Liu, G., & Xu, L. 2024, EPJC, 84, 934

Hu, J. P., Wang, F. Y., & Dai, Z. G. 2021, MNRAS, 507, 730

Hu, J. P. & Wang, F. Y. 2023, Universe, 9, 94

Izzo, L., Muccino, M., Zaninoni, E., Amati, L., & Della Valle, M. 2015, A&A, 582, A115

Jia, X. D., Hu, J. P., Yang, J., Zhang, B. B., & Wang, F. Y. 2022, MNRAS, 516, 2575

Jiang, Jun-Qian, Pedrotti, D., da Costa, S. S. & Vagnozzi, S. 2024, PRD, 110, 123519

Jimenez, R., Verde, L., Treu, T. & Stern, D. 2003, ApJ, 593, 622

Jiao, K., Borghi, N., Moresco, M. & Zhang, T-J. 2022, arXiv:2205.05701

Khadka, N. & Ratra, B. 2020, MNRAS, 499, 391

Khadka, N., Luongo, O., Muccino, M., & Ratra, B. 2021, JCAP, 09, 042

Kingma D. P.& Ba, J. 2014, arXiv.1412.6980

Kodama, Y., Yonetoku, D., Murakami, T., et al. 2008, MNRAS, 391, L1

Liang, E., & Zhang, B. 2005, ApJ, 633, 611

Liang, E., & Zhang, B. 2006, MNRAS, 369, L37

Li, X. and Lin, H.-N., 2018. MNRAS, 474, 313

Li, E.-K., Du, M., & Xu, L. 2020, MNRAS, 491, 4960

Li, X., Keeley, R. E., Shafieloo, A., et al. 2021, MNRAS, 507, 919

Li, Z., Zhang, B., & Liang, N. 2023, MNRAS, 521, 4406

Li, J.-L. et al. 2024, A&A, 689, A165

Liang, N., Xiao, W. K., Liu, Y., & Zhang, S. N. 2008, ApJ, 685, 354

Liang, N., & Zhang, S. 2008, AIP Conf. Proc. Vol. 1065, Am. Inst. Phys New York

Liang, N., Wu, P., & Zhang, S. N. 2010, PRD, 81, 083518

Liang, N., Xu, L., & Zhu, Z. H. 2011, A&A, 527, A11

Liang, N., Li, Z., Xie, X., & Wu, P. 2022, ApJ, 941, 84

Lin, H. N., Li, X. & Chang, Z. 2016, MNRAS, 455, 2131

Linder, E.V. 2003, PRL, 90, 091301

Liu, Y., Liang, N., Xie, X., et al. 2022, ApJ, 935, 7

Liu, J., & Wei, H. 2015, GReGr, 47, 141

Luongo, O., & Muccino, M. 2021, Galaxies, 9, 77

Luongo, O., & Muccino, M. 2021, MNRAS, 503, 4581

Luongo, O., & Muccino, M. 2023, MNRAS, 518, 2247

Ma, C. & Zhang T.-J. 2011, ApJ, 730, 74

Montiel, A., Cabrera, J. I., & Hidalgo, J. C. 2021, MNRAS, 467, 3239

Moresco, M., Verde, L., Pozzetti, L., Jimenez, R. & Cimatti, A. 2012, JCAP, 08, 006

Moresco, M. 2015, MNRAS, 450, L16

Moresco, M., Pozzetti, L., Cimatti, A. et al. 2016, JCAP, 05, 014

Moresco M., Jimenez R., Verde L., et al. 2020, ApJ, 898, 82

Muccino, M., Izzo, L., Luongo, O., et al. 2021, ApJ, 908, 181

Muccino, M., Luongo, O., & Jain, D., 2023, MNRAS, 523, 4938

Mu, Y., Li, E.-K., & Xu, L. 2023, JCAP, 06, 022

Mu, Y., Chang, B., & Xu, L. 2023, JCAP, 09, 041

Mukherjee. P. et al. 2024, JCAP, 09, 060

Mukherjee. P. et al. arXiv:2411.03773

Nong, X.-D. & Liang, N. 2024, RAA, 24, 125003

Pan, Y., Qi, J., Cao, S., et al. 2020, ApJ, 890, 169

Plank Collaboration. Aghanim, N., Akrami, Y., Arroja, F., et al. 2020, A&A, 641, A1

Ratsimbazafy, A. L., Loubser, S. I., Crawford, S. M. 2017, MNRAS, 467, 3239

Reichart, D. E. 2001, ApJ, 553, 57

Rubin. D. et al. arXiv:2311.12098

Riess, A. G., et al. 2022, ApJ, 934, 7

Schaefer, B. E. 2007, ApJ, 583, L67

Scolnic, D. M., Jones, D. O., Rest, A., et al. 2018, ApJ, 859, 101

Scolnic, et al. 2022, ApJ, 938, 113

Seikel, M., Clarkson, C., & Smith, M. 2012, JCAP, 06, 036

Seikel, M., Yahya, S., Maartens, R., & Clarkson, C. 2012, PRD, 86, 083001

Sethi, G., Sharma, U., & Makhijani, N. 2024, ApSS, 369, 42

Simon, J., Verde, L. & Jimenez, R. 2005, PhRvD, 71, 123001

Stern, D., Jimenez, R., Verde, L., Kamionkowski, M. & Starford, S. A. 2010, JCAP, 2010, 008

Salvaterra, R., & Valle, M., & Campana, S., et al., 2009. Nature, 461, 1258–1260

Shah, R., Saha, S., Mukherjee, P. et al. 2024, ApJS, 273, 27

Sun, W., Jiao, K., & Zhang, T.-J. 2021, ApJ, 915, 123

Tomasetti, E., Moresco, M. & Borghi, N. et al., 2023. A&A, 679 (2023) A96

Tang L., Li X., Lin, H.-N., & Liu L. 2021, ApJ, 907, 121

Wang, Y. 2008, PhRvD, 78, 123532

Wang, F. Y., Dai, Z. G., & Liang, E. W. 2015, NewAR, 67, 1

Wang, J. S., Wang, F. Y., Cheng, K. S., & Dai, Z. G. 2016, A&A, 585, A68

Wang, F. Y., Hu, J. P., Zhang, G. Q., & Dai, Z. G. 2022, ApJ, 924, 97

Wang G. J., Ma X. J., Li S. Y., Xia J. Q. 2020, ApJS, 246, 13

Wang, G. Z., Li, X. L. & Liang, N. 2024, ApSS, 369, 74

Wang, H. & Liang, N. 2024, MNRAS, 533, 743

Wei, H., Zhang, S. N. 2009, EPJC, 63, 139

Wei, H., 2010, JCAP, 08, 020

Wei, J.-J. & Wu, X.-F., 2017. ApJ, 838, 160

Xie, H., Nong, X., Wang, H., Zhang B., Li, Z., & Liang, N. 2024, IJMPD, 2450073, 20

Yonetoku, D., Murakami, T., Nakamura, T., et al. 2004, ApJ, 609, 935

Zhang, C., Zhang, H., Yuan, S., Liu, S., Zhang, T. & Sun, Y. 2014, RAA, 14, 1221

Zhang, J. C., Jiao, K., Zhang, T., Zhang, T. J., & Yu, B. 2022, ApJ, 936, 21

Zhang H., Liu, Y., Yu, H., Nong, X., Liang, N. & Wu, P. 2024, MNRAS, 530, 4493

Zhang J. C., Hu Y., Jiao K., Wang H. F., Xie Y. B., Yu B., Zhao L. L., & Zhang, T. J. 2024, ApJS, 270, 23

Zhang B., Wang, H., Nong, X., Wang, G., Wu, P. & Liang, N. 2025, ApSS, 370, 10